Materials & Design 212 (2021) 110259

Contents lists available at ScienceDirect

Materials & Design

journal homepage: www.elsevier.com/locate/matdes

Glass-ceramic sealants and steel interconnects: Accelerated interfacial stability and reactivity tests at high temperature

A. Drewniak [a,*], D. Koszelow [a], P. Błaszczak [b], K. Górnicka [b], K. Jurak [c], H. Javed [d], A.G. Sabato [e], P. Jasiński [a], S. Molin [a], F. Smeacetto [f]

[a] Faculty of Electronics, Telecommunications and Informatics, Gdańsk University of Technology, ul. G. Narutowicza 11/12, 80-233 Gdańsk, Poland
[b] Faculty of Applied Physics and Mathematics, Gdańsk University of Technology, ul. G. Narutowicza 11/12, 80-233 Gdańsk, Poland
[c] Faculty of Chemistry, Gdańsk University of Technology, ul. G. Narutowicza 11/12, 80-233 Gdańsk, Poland
[d] Sunfire GmbH, Gasanstaltstraße 2, 01237 Dresden, Germany
[e] Institut de Recerca en Energia de Catalunya (IREC), Jardins de les Dones de Negre, 1, 2ª pl., 08930 Sant Adrià de Besòs, Barcelona, Spain
[f] Department of Applied Science and Technology, Politecnico di Torino, Corso Duca degli Abruzzi, 24, 10129 Torino, Italy

HIGHLIGHTS

- Reactions between glass–ceramic sealants and Fe-Cr alloy interconnects at 750 °C and 850 °C.
- Sr-containing glasses are less reactive compared to the Ba-containing ones.
- Accelerated interfacial stability by exposing high surface area is reported for the first time.

GRAPHICAL ABSTRACT

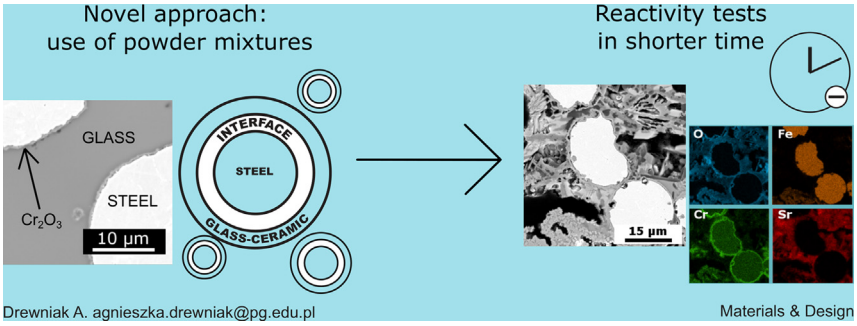

ARTICLE INFO

Article history:
Received 16 August 2021
Revised 16 November 2021
Accepted 17 November 2021
Available online 17 November 2021

Keywords:
Stainless steel powder
Glass–ceramic sealants
Reactivity
High temperature corrosion
Solid oxide cells
Interface

ABSTRACT

High-temperature reactions between glass–ceramic sealants and Fe-Cr alloy interconnects may lead to the formation of undesirable phases, and consequently degradation of solid oxide fuel/electrolyser devices. In this work, three different glass–ceramic sealants (Na-containing, Ba-containing, Sr-containing compositions) and Fe22Cr stainless steel powders (raw and pre-oxidised) are considered in order to test their chemical reactivity at 750 °C and 850 °C for 500 h in static air. The novelty of this approach is related to the use of powder mixtures instead of studying the reactivity on planar interfaces, which allows a better evaluation the materials' reactivity. Oxidation tests indicate that the Sr-containing glass–ceramic/steel couple is the least reactive among the aged samples. For the Ba-containing samples, the formation of an undesirable phase of $BaCrO_4$ is observed by diffractometry and photoelectron spectroscopy analyses. The present research explores, for the first time, the effects of exposing the high surface area of the alloy powder and glass–ceramic sealant interface, assessed by oxidation testing and microstructural analysis. The results show that by using mixed powders with large interface surface areas, degradation of the materials can be observed after relatively short times, allowing accelerated screening of the reactivity of materials, and thus their further development.

* Corresponding author.
E-mail address: agnieszka.drewniak@pg.edu.pl (A. Drewniak).

https://doi.org/10.1016/j.matdes.2021.110259
0264-1275/

1. Introduction

Due to the growing demand for green energy, ongoing efforts are underway to improve the lifetime and efficiency of the solid oxide-based electrochemical devices and materials. The ability to operate the solid oxide cells in two modes, i.e. as an electrolyser (SOEC) for energy storage, and as a fuel cell (SOFC) for energy generation, is an important advantage. These devices are particularly attractive because of the possibility of obtaining high efficiency for energy storage and conversion. However, the high working temperatures (700 °C – 900 °C) and the expected operating life of more than 40,000 h result in the degradation of stack components [1–5]. Therefore, it is important to select chemically and mechanically stable materials with similar thermal expansion coefficients (TECs) [6]. In addition, the device should be capable of operating under simultaneously applied reducing and oxidising conditions [7–11] and thermal cycles.

Typical cells for solid oxide cells (SOCs) applications consist of a porous anode, a dense electrolyte and porous cathode with a sandwich structure. Both the electrodes and electrolyte materials have been widely discussed in the literature [7,12–20]. Single cells are physically and electrically connected in stacks by interconnectors and the entire structure is sealed. Metallic interconnect are used due to high conductivity and low cost [17,21–23]. However, exposure to high temperature in working conditions leads to corrosion of the alloys [11,24–28] Therefore, it is possible to slow down the corrosion processes by pre-oxidation of the steel [27,29,30]. Hong et al. stated that metal pre-oxidation forms stable chromium oxide scale, hindering the reaction between glass and metal, moreover plays an important role in the bonding between the phases [31]. In addition, knowledge of the relationship between the structure and properties of the oxide and metal at their interface is important for technological applications such as anti-corrosion coatings and metal/ceramic composites [32].

A sealant is needed to prevent gas leakage and to provide electrical insulation between adjacent steel interconnects in the stack. Due to their properties, glass-ceramics are promising candidates for sealants at high temperatures. They exhibit good wettability on metal and ceramic substrates, and have high electrical resistance, ease of fabrication and low production costs. Moreover, their properties can be tailored by changing their composition [29,33,34].

Durable glass–ceramic/metallic interconnect joining requires good adhesion between the materials and comparable thermal expansion coefficients [8,19,29,33–43]. Special focus on the chemical composition of the glass–ceramic sealant is essential for long-term chemical and mechanical stability of the joint. Several degradation mechanisms are caused by phase changes, diffusion between elements or cracking, especially considering the harsh operating conditions (high T, oxidising and reducing atmosphere, applied electrical voltage and thermal cycles) [44]. Due to the thermomechanical properties, the reactivity at the metallic interconnect and glass–ceramic sealant interface should be as low as possible low [45]. Researchers have presented several papers on glass–ceramic sealants for SOEC and SOFC applications [34,41,46–50], dealing with different compositions and the resultant properties. The presence of different oxides significantly affects the properties of the sealant. For example, the commonly used Na_2O modifier improves the TEC, enhances wettability and reduces the viscosity of the glass, but has high reactivity and reduces the electrical resistivity of the glass–ceramic [51]. The use of BaO increases the TEC and reduces the glass transition temperature, but reacts with the chromium from the interconnect to form $BaCrO_4$, leading to stresses that can result in crack formation at the interconnector/sealant interface [29,41,52]. Similarly, the addition of SrO adjusts the TEC and improves wettability, but SrO-containing glass-ceramics also suffer from the formation of a high TEC $SrCrO_4$ phase [29]. Nevertheless, the Sr-based glasses have less tendency to form $SrCrO_4$ as compared with $BaCrO_4$ in Ba-based glasses. [53–55].

In this work, a total of six sample types were prepared. Each of them consisted of previously designed glass–ceramic sealants (V11, HJ4 or GC2) and a Fe22Cr stainless steel powder (SSP) - raw or pre-oxidised. To the best of our knowledge, only one research work about joining glass and steel powder was described - Sander et al. melted blends of 316L stainless steel powder and glass by selective laser melting [56]. However, their approach resulted in "alloying" and was studied in an entirely different context. Microstructure studies and ageing tests were carried out at the typical operating temperature of solid oxide cells (750 °C or 850 °C). The aim of the study was to determine whether the use of stainless steel powder can provide additional information about the reactivity of compounds at the metallic interconnector and glass–ceramic sealant interface. The test method used is based on investigation samples consisting of stainless steel powder and glass–ceramic mixed together.

The new approach, proposed in this study for the first time as a an accelerated test method, using extended specific surface areas, has provided a deeper insight into glass–ceramic and metallic interconnect interfacial reactions in SOC device. A further study could assess the long-term effects of different interfacial reactivities by considering possible weakness and limitation of this approach. Specifically, experimental conditions may need a more detailed experimental assessment, i.e. different environment as a harsh reducing and oxidizing atmosphere in the working condition of a real single repeating unit in a SOC stack.

The main advantage of such a novel approach is the ability to perform reactivity tests in a much faster time compared to testing traditional planar metallic interconnect and glass–ceramic sealant interfaces. Different glass-based sealant compositions plays a crucial role in determining interfacial stability with the metallic interconnects. No previous study has investigated different families of glass-based sealants in contact with the same interconnect materials. This paper explores, for the first time, the effects of possible corrosion mechanisms, depending on the different glass modifiers, at high temperatures in accelerated conditions.

2. Experimental

Commercial Sandvik Osprey 1C44Mo20 (Fe22Cr) stainless steel powder (SSP), batch no. 09D0585, was wet fractionated in isopropanol by Retsch test sieves with screens with openings sized 38 μm and 20 μm on a Multiserw LPzE-2e sieve shaker. For this study, only one fraction (20 +), made up of particles bigger than 20 μm, was selected for forming the composite. The obtained powder was divided into two parts – one was left raw while the other was pre-oxidised. For pre-oxidation, the powder was placed in alumina crucibles and exposed to 850 °C in static air for 10 h. The weight gain due to pre-oxidation was ~ 4.5%. Particle size distribution (PSD) were measured by Beckman Coulter LS 13–320 laser diffraction system and the specific surface area (SSA) was obtained by physical by Quantachrome Instruments Autosorb iQ apparatus with nitrogen gas measured by Brunauer-Emmett-Teller physical adsorption model method. Information about PSD and SSA are given in Table 1. Chemical composition of the alloy powder was given by producer and compared with EDS analysis in Table 2.

Three previously developed (at Politecnico di Torino, Italy) glass-ceramics further labelled as V11 (Na-containing), HJ4 (Sr-containing) and GC2 (Ba-containing), were used to investigate their chemical reactivity with the Fe22Cr stainless steel powder

Table 1
Fe22Cr powder particles parameters.

SSP parameters					
Fe22Cr	Median [μm]	d_{10} [μm]	d_{90} [μm]	mode [μm]	SSA [m^2g^{-1}]
20+	28.72	21.66	38.44	30.07	0.055

Table 2
Fe22Cr powder chemical composition

SSP chemical composition [wt.%]													
Fe22Cr	Fe	Cr	Mn	Si	Ni	N	Mo	Nb	Co	V	Cu	P	S
Target composition	Bal.	22	Max. 0.4	0.25	0.4	0.4	0.8–1.2	0.6–0.9	Max. 0.015	Max. 0.1	Max. 0.01	Max. 0.015	Max. 0.01
EDS	76.02	22.56	0.29	0.56	0.08	0.16	0.41	–	–	–	–	–	–

particles. The chemical compositions of the glasses are given in Table 3. The used designations of the composite samples are: Na-R, Na-P, Ba-R, Ba-P, Sr-R, and Sr-P, where Na/Ba/Sr refer to the glass modifier-element and the R/P denote either a raw (R) or pre-oxidised (P) steel powder used.

The composite glass–ceramic/stainless steel samples were prepared by mixing the powders in a 50 : 50 vol ratio for 5 min in an agate mortar. Due to the significant differences in the densities of the steel (7.7 g/cm^3) and glasses (~2.9 g/cm^3), the samples were prepared using volume ratios instead of weight ratios. This made it possible to obtain a good dispersion of the steel powder in the glass/ceramic. The prepared powder mixture was placed in a hardened steel die with an internal diameter of 6 mm and subjected to a hydraulic press with a pressing force of 0.5 ton (173 MPa) for 60 s. Subsequently, the obtained pellets were placed in a furnace (Linn High Therm muffle furnace) for 2 h at the temperature of 850 °C (Na-R/P) or 950 °C (Ba-R/P, Sr-R/P) in a static air atmosphere. The heating and cooling rate was 5 °C/min. This first heat treatment step corresponds to typical joining procedures of these glasses. For each sample type, 5–10 pellets were prepared to allow the reproducibility to be assessed.

High-temperature exposures (oxidation) of the composite pellets were performed in a tube furnace with a quartz tube (50 mm outer diameter, 40 mm inner diameter). The pellets were placed on alumina (99.7%) substrates and inserted into the furnace and heated up to the test temperature (750 °C for Na-R/P, 850 °C for Ba-R/P, Sr-R/P). The samples were exposed cyclically (30 h, 70 h, 150 h, 250 h) for a total time of 500 h with intermediate cooling and weight measurement. The heating procedure was set to 5 °C/min until the selected temperature was reached, cooling was performed at the same rate until room temperature was reached. Measurements were performed in a stagnant air atmosphere. Weight gain measurements were performed on a Radwag XA 6/21.4.Y.M.A.B. PLUS microbalance. The heat treatment procedures are summarised in Table 4.

To ensure reproducibility and validity of the experiments, additivity tests have been carried out - by testing samples of different weights and sample sizes, comparing areas close to the surface with the center of the powder mixture and the results were found to be in good agreement. For very large mass gains, i.e. for steel powder that has undergone breakaway corrosion, there are geometric problems for the growing oxide.

Table 4
Heat treatment parameters of the samples

Heat treatment parameters [°C]			
	Na-R/P	Sr-R/P	Ba-R/P
Initial heat treatment temperature (2 h) [°C]	850	950	950
Oxidation temperature (500 h) [°C]	750	850	850

After the exposures at high temperatures, phase identification was performed on grounded samples by X-ray diffractometry (XRD) using a Bruker D2 Phaser XE-T with CuK_α radiation at room temperature. The measurements were performed in the Bragg-Brentano 2θ configuration over the range of 20–90°.

The x-ray photoelectron spectroscopy (XPS) tests were performed on a Thermo Fisher Escalab 250Xi apparatus and Thermo Avantage software for analysis. AlK_α radiation was used, and the spot size was 900 μm. The samples were prepared in the form of grounded powder on carbon tape. XPS identification was performed for the core spectral region. Curve fitting with the Voigt function was used. Due to the ferromagnetic nature of the tested samples and the related measurement difficulties, the signal-to-noise ratio is relatively high, but sufficient for the observation of changes due to chemical reactivity as a qualitative method [58,59]. The photoelectron emission peaks (BE), full widths at half maximum (FWHM), lineshapes, and backgrounds were determined.

The microstructures of the samples were analysed with a Phenom XL scanning electron microscope (SEM) and a Thermo Fisher Scientific Silicon Drift Detector energy dispersive X-ray spectroscope (EDS). The samples' surfaces and polished cross-sections (Struers EpoFix epoxy and polished up to 1 μm by a Struers Tegramin system) were analysed.

3. Results and discussion

3.1. Materials selection and initial characterisation

Sandvik Osprey 1C44Mo20 alloy was selected for this study, since its chemical composition (Cr content ~ 22 wt%) matches

Table 3
Glass-ceramics chemical composition

Glass-ceramics chemical composition [wt.%]										
	SiO_2	CaO	Al_2O_3	ZrO_2	B_2O_3	SrO	Y_2O_3	Na_2O	MgO	BaO
V11 [41]	46.37	14.34	8.34	2.92	5.76	–	–	9.26	13	–
HJ4 [53]	57.6	–	6.17	–	5.65	28.84	1.74	–	–	–
GC2 [57]	55	7	4	–	8	–	–	–	–	26

state-of-the-art alloys used in Solid Oxide Cell stacks and is thus a good model material to study reactivity with glass–ceramic materials.

The steel powders were used in either raw or pre-oxidised form. The pre-oxidation procedure produces a thin, well defined and adhering layer of chromium oxide covering the metallic particles. These two treatment procedures were selected to highlight any possible influence of chromia scale on the reactivity of steel. Depending on the specific stack design, during its assembly (e.g. protective coatings preparation), the sealing areas of the interconnects might be either in the bare-metal or initially oxidised form.

The studied glass–ceramic sealants were initially designed for SOFC/SOEC application having different working temperatures, i.e. the HJ4 and GC2 glass-ceramics at 850 °C, and the V11 glass–ceramic at 800 °C. All of the glass-ceramics are silica-based (SiO_2) systems with different types of modifiers, i.e. HJ4 contains Sr, while GC2 and V11 contain, respectively, Ba and Na as main modifiers, which can result in different reactivity with steel. The glass compositions and heat treatment procedures were selected to obtain similar TECs as metallic elements, and to reduce the thermal stress at the glass–ceramic and metal interface. The glass TEC values are, respectively, 12.8 × 10^{-6} K^{-1} for V11 glass [41], 9.6 × 10^{-6} K^{-1} for HJ4 glass [53] and 11.4 × 10^{-6} K^{-1} for GC2 glass [57], while ∼ 12 × 10^{-6} K^{-1} is the value for chromia-forming alloys [60]. More information on the preparation and synthesis of glass powders are available in the literature [41,53,61].

The microstructures of the surfaces and cross-sections of the as-prepared samples (2 h initial heat treatment) were analysed by SEM and the results are presented in Fig. 1. Each image was taken at a magnification of 10 kx to highlight the interface between the steel particles and the glass (lower magnification images are presented in Figure S1). The Na-R sample showed a well-adhered, thin layer of chromium oxide on the surface of the steel particles, with pitting at the grain edges. The image of the Na-P sample showed similarity, however, the chromium oxide layer was ∼ 2x thicker than that of the Na-R. Moreover, both images showed a porous, amorphous structure of V11 glass with numerous crystallites formed. The steel powder particles of the Sr-R sample contained a thin layer of Cr_2O_3 adhering to its smooth surface. No pitting or discontinuity in the oxide structure was observed, but the presence of pores at the Cr_2O_3/SSP interface was noted. In the case of the Sr-P sample, a rough surface of the SSP was observed, and the very well adhered chromium oxide had a thickness of ∼ 2x greater than that of the sample made with the use of the raw, non-pre-oxidised powder. The Sr-R/P samples, after preliminary heat treatment, showed an almost completely amorphous structure of HJ4 glass. As in the case of the previously discussed samples (Na-R/P, Sr-R/P), Ba-R and Ba-P also differ in the thickness of the chromium oxide layer, but the difference is not that significant. This is related to the formation of a new phase, recognised as barium chromate ($BaCrO_4$), the presence of which was confirmed by the studies discussed later. A large proportion of the chromium was used to form $BaCrO_4$, hence a reduced amount of chromium oxide on the SSP surface is noticeable. Apart from the visible $BaCrO_4$ phase formed around the steel powder particles, the GC2 glass remained mainly amorphous. The dark spots visible in the SSP in Na-P and Ba-R are locally Cr enriched phases, e.g. oxides/nitrides.

Figure S1 shows that the stainless steel powders were evenly dispersed in the glass–ceramic. The glass-ceramics showed a homogeneous microstructure with some pores and other defects with residual amorphous phases. Despite the pores in glass-ceramics phase, strong bonding and compatibility with the powder particles were visible (excluding the V11 samples). The samples from the V11 series turned out to be the most crystallised and the most porous. In the previous investigation, V11 glass also showed porosity and locally good adhesion [41]. The structure of the HJ4 series was of an opposing character, it had the smallest amount of large pores, and mainly the residual amorphous phase of glass was observed. Previous studies on the HJ4 glass–ceramic system also showed that it maintains a considerably high content of residual glassy phase after the joining treatment [53].

3.2. Oxidation test results

Interconnect steels subjected to high temperatures form chromium oxide scale on the surface. The kinetics of oxidation can be studied by weight gain measurements. To assess the influence of the glass-ceramics on the oxidation kinetics, cyclic thermo-

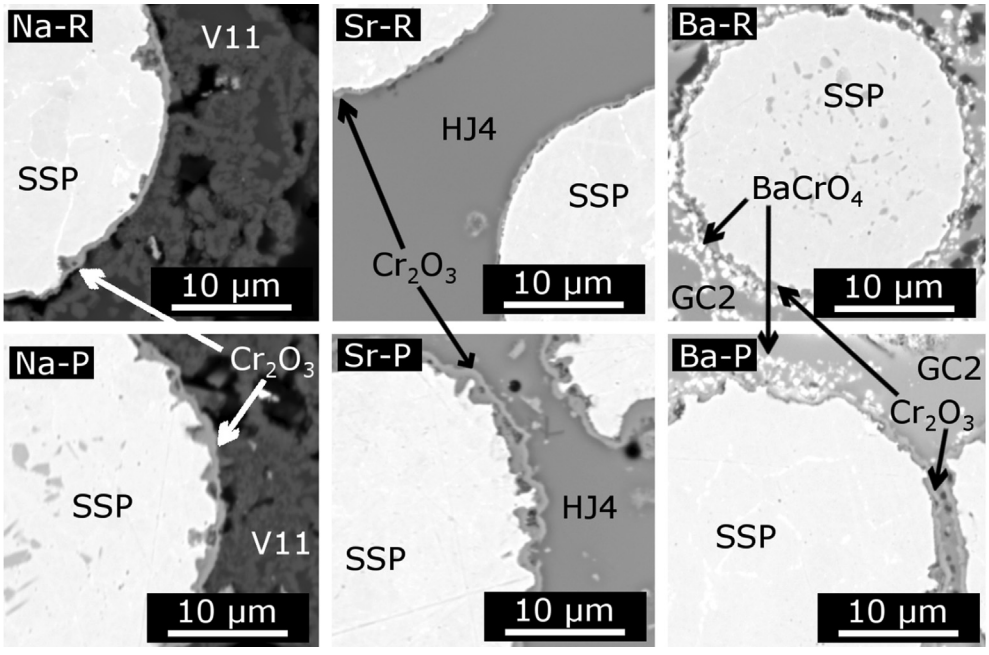

Fig. 1. Back-scattered SEM images of cross-sections of the as-prepared samples (2 h initial heat treatment).

gravimetry exposures were carried out for the composite and raw alloy powder samples.

Fig. 2A shows the weight gain at 750 °C for the raw powder and Na-R/P composite samples. The weight gain of the pure stainless steel powder was higher than the weight gain of the steel powders mixed with the glass–ceramic. The weight gain of the Na-R samples was roughly one third (1.43%) of reference sample weight gain in the same temperature, whereas the weight gain of the Na-P was even smaller (0.61%), due to the initial formation of the protective oxide scale. During the first 250 h, the weight gain of the steel particles – glass–ceramic samples increased gradually, achieving ~ 2.2 %, and then rapidly accelerated and achieved over 19% in the following cycle.

Fig. 2B shows the weight gain plots of pure steel powder, and Ba-R/P and Sr-R/P samples oxidised at 850 °C. As expected, the weight gains at higher temperature are higher.

After 500 h of oxidation, the Ba-P sample proved to be the most susceptible to oxidation, achieving a weight gain of 14.3%, and the most oxidation resistant was the Sr-R sample, achieving a low weight gain of 2.94%. A possible explanation for this is that samples Sr-R/P and Ba-R/P are less porous than Na-R/P. Interface adhesion is a key aspect in both test systems and real systems, the porosity of one of the materials is a factor affecting the quality of the joint, especially at the interface. Due to the obstructed supply of oxygen, the growing oxide has no physical space for further growth, regardless of whether the metallic particle had a passive layer or not. In the case of Ba-R/P, a great deal of chromium is used up in the formation of barium chromate. Moreover, both the joining and ageing temperature are 100 °C higher for the Sr-R/P and Ba-R/P-series samples compared to the Na-R/P series, which greatly increases the rate of oxidation of the steel particles. The pre-oxidised samples achieved greater weight gain.

The reference samples showed significantly greater degradation at high temperatures. After 30 h of exposure to the temperature of 850 °C, breakaway corrosion occurred, and its further growth was exempted by geometric considerations. Also in the tests at 750 °C, the SSP reference samples achieved several times greater values of weight gain.

In Fig. 2, the relative weight gains of Na-R/P, Ba-R/P, and Sr-R/P are a weight gain of mixtures. For a more direct comparison with the reference sample, the same data are presented with recalculated weight gain (as a weight gain of SSP in the mixture) and is presented in Figure S.2. in supplementary materials. It was assumed that the total weight gain comes from the oxidation of the SSP, and from the glass–ceramic is negligible. Using the SSP and glass–ceramic density values, a coefficient of 0.73 was calculated.

SEM images of the samples after 100 h are presented in Fig. 2:1–5 and also in Figures S3 (Na-R/P), S4(Sr-R/P), S5 (Ba-R/P).

The microstructure of the pure steel after 100 h of oxidation (weight gain of ~ 4.1%.) is presented in Fig. 2-1. It shows ~ 25 μm steel particle with a thin layer of oxide scale (<1 μm). For the mixed sample, the amount of the steel powder (~50 vol%) results in a lower weight gain due to oxidation of a smaller amount of the steel particles.

Fig. 2-2 presents the Na-R sample, where a ~ 20 μm steel particle surrounded by the V11 glass is visible. The steel particle formed some internally growing oxide in places in contact with the glass–ceramic phase.

Fig. 2:2–4 show an increased proportion of crystalline phases in the glass–ceramic compared to the as-prepared samples (Fig. 1) and a more pronounced oxide scale layer forming on the surface of the steel powder.

Fig. 2:5 shows the fully oxidised stainless steel particle – complete transformation of the chromium and iron to their oxide forms.

3.3. Post mortem analysis

3.3.1. XRD analysis

Typically, XRD analyses of steel-glass systems are limited by a small planar interface area, covered with glass on steel with oxidation products in between. This geometry makes the analysis inconvenient as it is hard to probe the interface, and the signals can be attenuated depending on their depth. In the case of analysis of high-surface-area powders proposed in this work, the phases can be analysed accurately.

XRD analyses for the samples before and after oxidation (500 h) are shown in Fig. 3 and the results are collected in Table 5. The

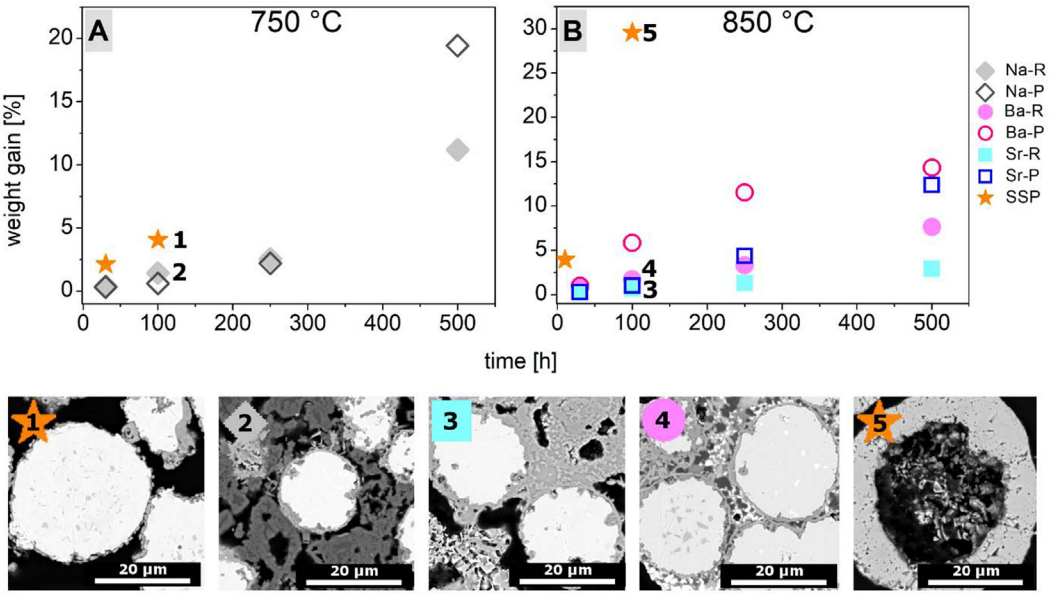

Fig. 2. Weight gain versus time plots of the V11 series aged 500 h at 750 °C in the air (A) and HJ4 and GC2 samples aged 500 h at 850 °C in the air (B) and SEM images of samples from the numbered (1–5) points.

diffractograms of the samples after 0/100/250/500 h are also presented in Figure S.6.

All diffractograms show peaks form the Fe22Cr steel – represented by $CrFe_4$ phase (JCPDS-ICDD PDF#65–4664, the most intense peak of the diffraction patterns at ~ 44.5°) coming from the alloy particles in the mixtures. As the ageing progresses, these reflections lose their intensity. In the case of the Na-P sample, the peaks from the $CrFe_4$ phase disappear, due to full oxidation of steel particles. This is related to the oxidation phenomenon leading to the depletion of chromium and iron from the structure of the metallic particles. The depletion of the Cr and Fe of the stainless steel powder enables the interaction of these elements with glass-ceramics.

The diffractograms of the Na-R/P samples show that diopside ($CaMgSi_2O_6$, PDF#71–1067) and nepheline ($NaAlSiO_4$, PDF#35–424) are the main crystalline phases. These phases improve the mechanical stability of the parent glass. The occurrence of nepheline in the V11 glass was previously observed, and these results are consistent with data obtained by Ritucci et al. [41].

The HJ4 glass contained mostly $SrSiO_3$ (PDF#24–1232) and $SrAl_2Si_2O_8$ (PDF#37–462) crystalline phases, and did not react with the metallic steel particles or chromium and iron oxides throughout the test. The occurrence of strontium silicate and cristobalite in the HJ4 glass was previously observed by Javed et al. [53]. There was no reduction in the intensity of the $CrFe_4$ peak after 500 h of oxidation in the SRR sample. This is consistent with the results from the weight gain test.

The GC2 glass reacted with the steel powder as early as at the mixing stage, resulting in the formation of $BaCrO_4$. The formation of barium chromate as a result of a chemical reaction between the Ba from the glass and the Cr from the steel is a previously observed phenomenon [57,62,63]. A large TEC mismatch between the barium chromate, sealant and ferritic steel can cause stress at interface, which would critical for the long-term stability of the SOFC/SOEC stack.

3.3.2. XPS analysis

To further resolve the potential phases and reactivity, an XPS analysis of the grounded powder samples (after 0 h and 500 h) was performed.

Table 5
Phase identification of the samples obtained from XRD analysis

Phase identification			
	Na-R/P	Sr-R/P	Ba-R/P
initial GC phases	$CaMgSi_2O_6$ $NaAlSiO_4$	SiO_2 $SrSiO_3$ $SrAl_2Si_2O_8$	$BaSi_2O_5$
initial SSP phases	$CrFe_4$ Cr_2O_3 $Fe_2O_3FeCr_2O_4$		
Post-reaction phases			$BaCrO_4$

XPS, as a surface analysis technique, would be challenging to perform on a steel/glass–ceramic planar sample. The depth of the analysis is up to 10 nm, therefore it would be difficult to reach the interface between steel and glass-ceramics. The advantage of the proposed analysis method is the possibility of using ground pellets, thanks to which we obtain a large interface area between the metallic powder and glass-ceramics.

Selected data from the XPS analyses are shown in Fig. 4 and Fig. 5. The main focus was placed on the binding energies of Cr and the most important elements from the point of view of chemical reactivity (Na – Na-R/P, Sr – Sr-R/P, Ba – Ba-R/P).

In Fig. 4, the binding energy values of chromium compounds are presented. The results of the XPS analysis are significantly different for all three types of tested composites. Two rather wide peak doublets were observed for the samples from the Sr-R/P, with binding energies characteristic of Cr^{3+}. According to the literature, native oxide on Cr metal may be a mix of Cr (III) oxide and Cr (III) hydroxide [64,65]. Composites made of pre-oxidised metallic particles and HJ4 glass, both before and after ageing, showed a greater proportion of chromium oxide than chromium hydroxide. The peak related to Cr_2O_3 has a greater intensity and this advantage grows with the ageing of Sr-containing samples.

The peaks for the Ba-R/P samples are even wider, with their maximums shifted towards higher binding energies than with the Sr-R/P. In this case, a model consisting of three doublets was fitted. Most likely, two of them again correspond to Cr_2O_3 and Cr $(OH)_3$ (Cr^{3+}), but Cr $2p_{3/2}$ 580 eV is the typical energy value of Cr^{6+} [64,65]. In the literature, it also appears as a value for $BaCrO_4$,

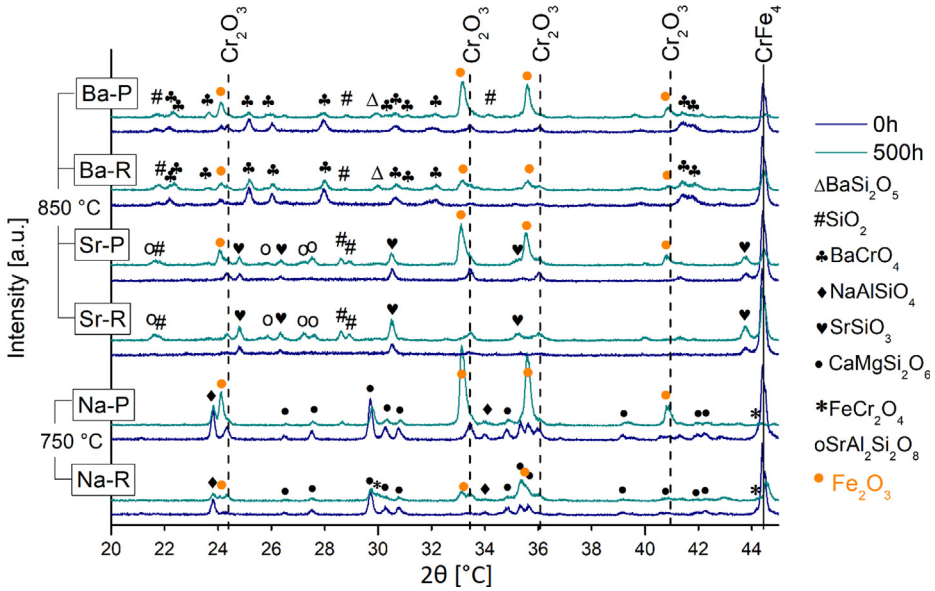

Fig. 3. XRD patterns of Na-R/P, Sr-R/P and Ba-R/P series before and after ageing (500 h in the air).

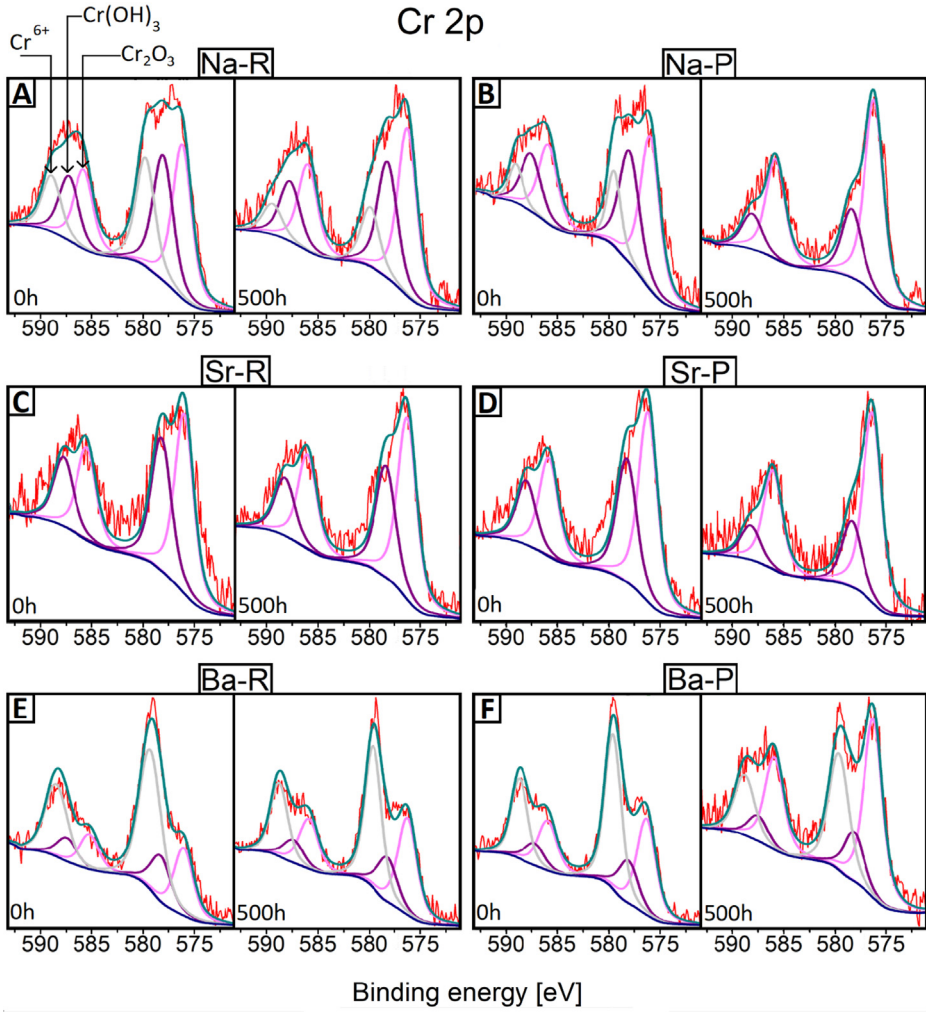

Fig. 4. XPS spectra for Cr 2p of Na-R/P, Sr-R/P and Ba-R/P series before and after ageing (500 h in the air).

which is consistent with the XRD and EDS results of the Ba-R/P samples [66].

Samples from the V11 series again indicate the presence of two components, most probably Cr^{3+} in the form of $Cr(OH)_3$ around 577.3 eV, and Cr^{3+} in the form of Cr_2O_3 at around 576.1 eV. However, in this case, a shift towards Cr^{6+} is also observed. It is quantitatively smaller than the spectrum defined as Cr_2O_3, but it is non-negligible. The content of Cr^{6+} decreases with the progress of ageing. The probable source of the Cr^{6+} peak is the formation of a small amount of Na_2CrO_4 (Cr $2p_{3/2}$ component at 580.5 eV).

Fig. 5 shows the XPS spectra of Na 1 s (Na-R/P samples), Sr $2p_{3/2}$ (Sr-R/P samples) and Ba $3d_{5/2}$ (Ba-R/P).

Sodium is detected in the XPS spectrum in the form of various compounds. A note of caution is due here, since, due to the superimposition of various sodium compounds in the same energy range of the binding energy, it is easy to make a mistake in interpretation. Furthermore, the binding energy may be influenced by the amorphous structure of the glass, therefore some peaks may appear shifted. We consider this result as inconclusive, however a slight shift of the peak to the right from 1071 eV (Fig. 5A&D) may indicate confirmation of the presence of sodium chromate. The widening of the peak as ageing progresses suggests chemical changes in the sodium state.

The formation of Na_2CrO_4, which is volatile at typical SOC operating temperatures, can be particularly detrimental since it leads to the degradation of the integrity of the glass–ceramic. Furthermore, sodium chromate is originated by the reaction between Na_2O or NaOH and Cr-containing species such as Cr_2O_3 or $CrO_2(OH)_2$, thus possibly compromising the corrosion-resistance of the steel [67–69].

The presence of two peaks for Sr 3d with a separation of ~ 2 eV comes from spin-orbit interaction (Sr $3d_{5/2}$ and $3d_{3/2}$). Two doublets were fitted, which, according to the literature, most likely correspond to the initial phase of the SrO glass [70] and the $SrCO_3$ + $SrSiO_3$ mix [71,72]. The binding energy (BE) shift is negligible for all four samples. Along with the ageing of the samples, the quantitative proportion of the amorphous SrO phase decreases in favour of the crystalline $SrSiO_3$ phase. These results confirm previous analyses of Sr-R/P samples and demonstrate the lack of reactivity of the metallic particles and the Sr-based HJ4 glass.

XPS analysis of samples from the Ba-R/P series for the core-level binding energy Ba 3d region showed the presence of both the initial BaO and the reacted $BaCrO_4$ phase. Due to similar binding energies, they were fitted to one peak (~779.5 eV). The peak at higher energy (~780.5 eV) corresponds to the $BaCO_3$ that may form due to sample ageing [71]. The quantitative proportion of chromate increases with the ageing process. Also, in this case, the curve shifts are marginal.

The results of the XPS analyses showed that using composites of steel powder and glass–ceramic enables the determination of the chemical states of the interfaces between steel and glass-ceramics. The results of the XPS spectrum analysis turned out to

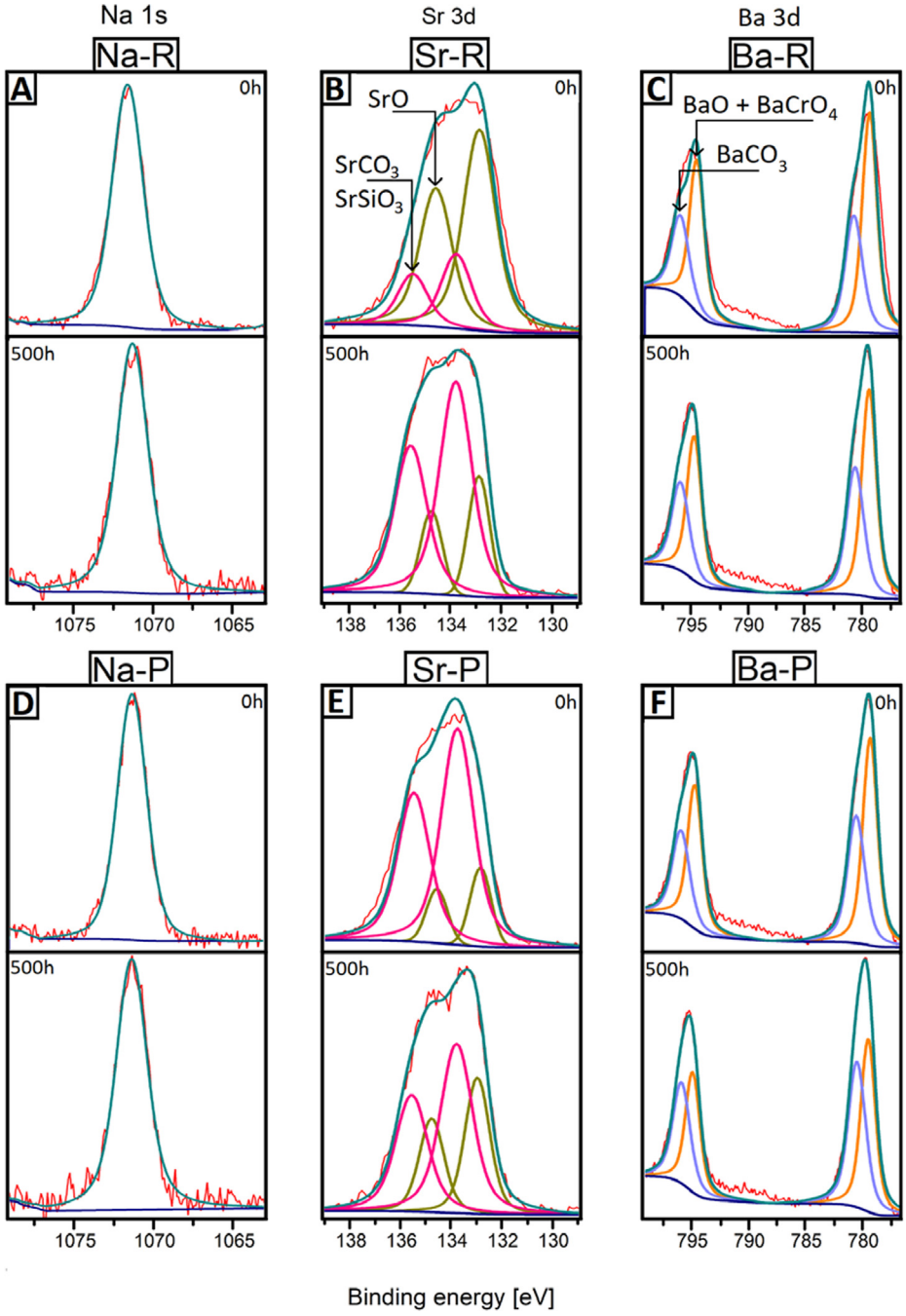

Fig. 5. XPS spectra of Na 1 s, Sr 3d and Ba 3d for Na-R/P, Sr-R/P and Ba-R/P series before and after ageing (500 h in the air).

be consistent with the results of the XRD analysis, which confirms the applicability of our new approach to SSP/G-C interface stability investigation.

3.3.3. SEM + EDS analysis

To determine the microstructure differences between the initial and aged samples, SEM/EDS analyses of polished cross sections were performed.

Fig. 6 shows the polished cross sections of the Na-R/P samples, before and after the ageing tests. In both as-prepared samples of Na-R/0h (Fig. 6.a.) and Na-P/0h (Fig. 6. b.), the steel powder was strongly bonded to the glass–ceramic only locally. The Cr signal appears to be stronger on the boundary of the metallic particles depicted in Fig. 6B, this was due to the pre-oxidation of the particles before to the joining treatment. After ageing of both samples (Fig. 6C and Fig. 6D), significant chromium and iron depletion in the metallic grain was observed. The overlapping between the O, Fe, and Cr maps clearly highlight the development of breakaway corrosion. Iron-rich oxide appears to be grown outside the particles in the space left by the porosities. Indeed, the elements of the glass–ceramic appear to be separated from these ones. These effects can be due to the formation of Cr-containing volatile species, enhanced by the presence of Na in this glass system, as discussed earlier in this section [67]

However, comparing Fig. 6C and D, the pre-oxidation seems to not have limited the oxidation of the inner core of the metallic particle. Furthermore, the Cr-containing oxide present outside the particle seems richer in Cr than in Fe, while, in the case of the

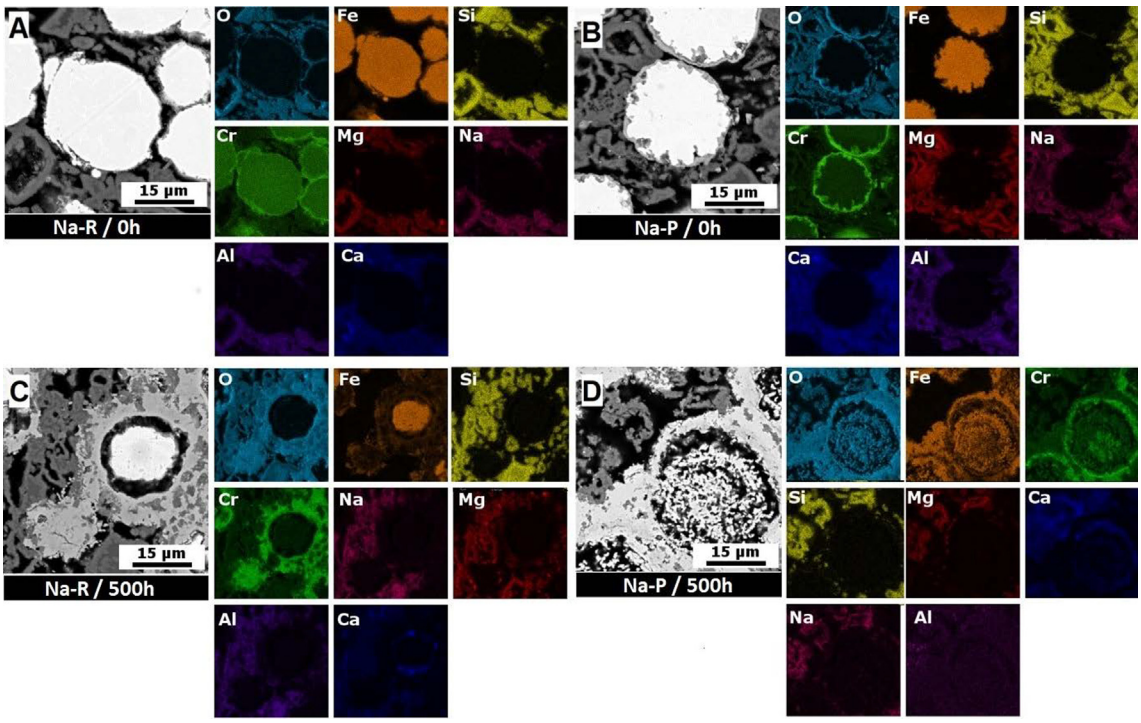

Fig. 6. SEM-EDS post mortem analysis of Na-R/P samples before (A,B) and after ageing (C,D).

pre-oxidised sample (Fig. 6D), the core of the metallic particles appears to be completely corroded.

In Fig. 7A and Fig. 7B, good adhesion between the steel powder and the HJ4 glass-ceramics series is visible. In both cases, a homogeneous, dense and almost completely amorphous structure of the HJ4 glass–ceramic can be observed. In the case of the sample containing pre-oxidised alloy powder, more crystalline phases can be seen. The glass–ceramic phases in the samples after 500 h of exposure to 850 °C are almost completely crystallised and also differ significantly from each other. In contrast to the Sr-R/500 h sample (Fig. 7D), the Sr-P/500 h sample (Fig. 7D) shows almost completely oxidised steel particles. Despite the full oxidation of the alloy, there was no formation of new phases, as determined by XRD and the presented SEM/EDS analyses.

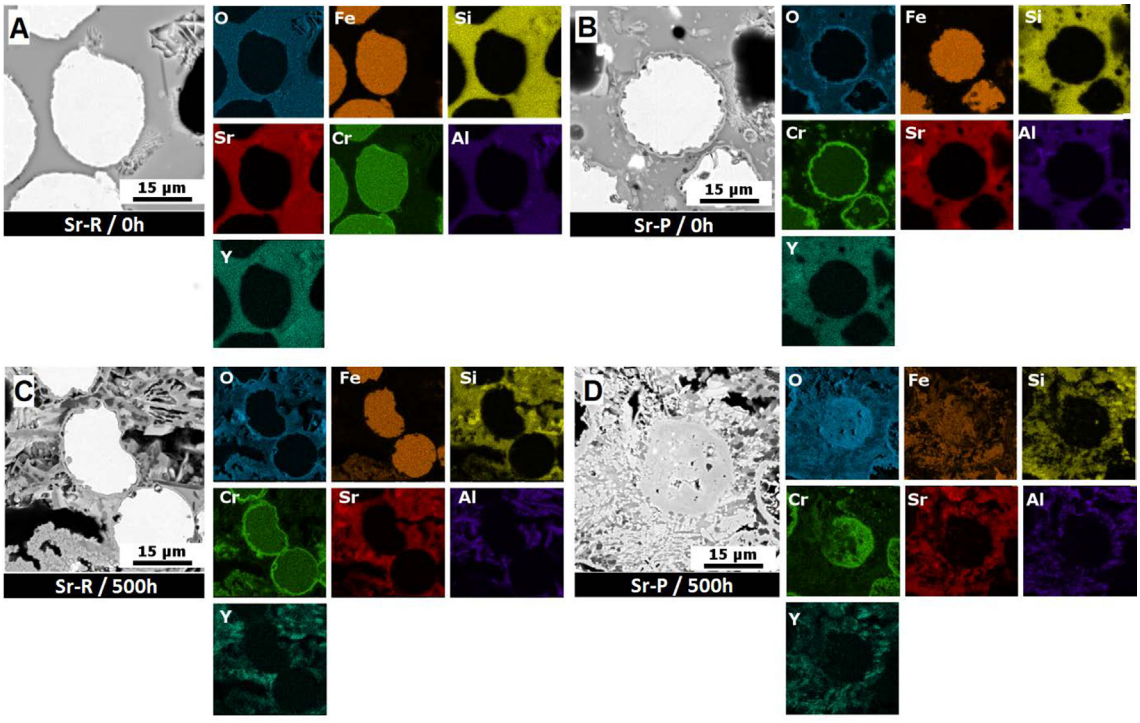

Fig. 7. SEM-EDS post mortem analysis of Sr-R/P samples before (A,B) and after ageing (C,D).

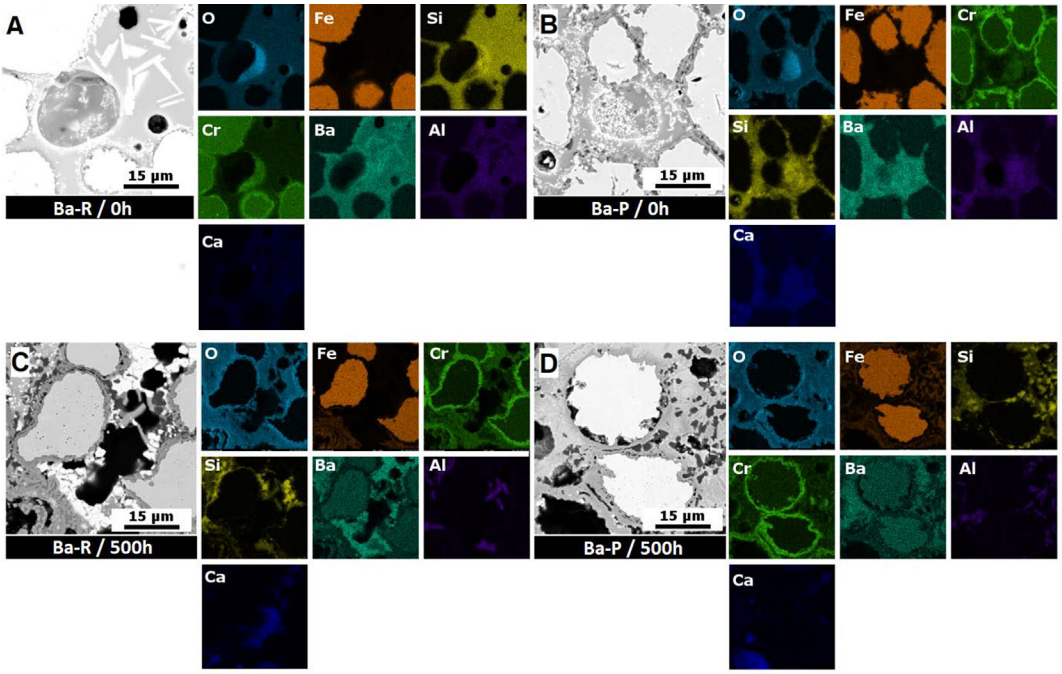

Fig. 8. SEM-EDS post mortem analysis of Ba-R/P samples before (A,B) and after ageing (C,D).

Polished cross-sections of the Ba-R/P are shown in Fig. 8. As with the as-prepared Sr-R/P samples, the Ba-R (Fig. 8A) and Ba-P (Fig. 8B) samples exhibited a strongly bonded glass–ceramic/steel powder interface. Similarly, the surrounding structure of the metallic grain consisted mainly of an amorphous phase with few crystalline precipitates. After only initial heat treatment (2 h at 950 °C) of the sample, the formation of small crystallites of $BaCrO_4$ could be observed in the vicinity of the steel particles. As shown in Fig. 8C and Fig. 8D, this phenomenon progresses with exposure time. On the Ba/Cr-EDS map, areas associated with the formation of barium chromate can be seen. In the SEM image, barium chromate is visible as bright white crystallites at the interface. The performed EDS analyses are consistent with both with the oxidation kinetics and the XRD, and XPS results.

Tests of Sr-R/P glass confirmed that Sr-based glasses are more stable and less chemically reactive compared to Ba-based and Na-based glasses [51]. Moreover, the conducted ageing tests show that the pre-oxidation of steel particles does not guarantee their longevity in the operating environment of the SOFC/SOEC from the point of view of the mass gain. However, pre-oxidation may be useful to enhance the wettability of the glass-based sealants on the metallic interconnects and to limit the formation of a detrimental reaction between these materials. Smeacetto et al. [41] successfully tested Na-containing glass-ceramics in contact with pre-oxidised Corfer22APU without any evidence of breakaway corrosion or reaction at the interfaces.

4. Conclusions

In this work, the reactivity of three different glass–ceramic materials (V11, HJ4, GC2) in contact with Fe22Cr stainless steel powder was investigated by a novel method involving powder mixtures. The high area of the materials interfaces facilitates the analyses by means of SEM, EDS, XRD, and XPS. The results of all of these analyses prove the viability of the method and show that this novel approach is suitable to prepare a model system for accelerated tests of alloy-ceramic reactivity.

All types of glass-ceramics samples after initial heat treatment showed the amorphous phase as the prevalent phase in the glass-ceramics. The Na-R/P samples showed a quite porous microstructure after bonding, whereas the remaining samples (Sr-R/P and Ba-R/P) were well bonded without pores and fractures at the surface of the stainless steel powder particles.

Comparing the materials containing either the raw (R) or pre-oxidised (P) powders, the pre-oxidised series were more susceptible to the damaging effects of high-temperature oxidation, possibly due to higher Cr-consumption by initial oxidation. Only the Sr-R samples showed no breakaway corrosion after 500 h.

Due to the powder nature of the materials, it was possible to perform XRD and XPS analyses, which are typically problematic for planar interfaces. The results were consistent and allowed for a better observation and understanding of the chemical reactivity processes.

Reaction and new phases formation were observed in the Ba-R/P samples, including barium chromate, resulting from the combination of glass-ceramics and stainless-steel powder (Ba-R/P), which can cause damage to the interface between glass-ceramics and metallic components. The Sr-R/P samples showed no reactivity with the Fe22Cr steel powder and good resistance to high temperature corrosion. Thus, it turned out to be the most promising seal material for SOC technology applications.

The experiments showed that Sr-containing samples are more stable and less chemically reactive compared to the Ba-containing materials. Moreover, the conducted ageing tests show that the pre-oxidation of steel particles does not guarantee their extended lifetime in the operating environment of the SOFC/SOEC, and some other strategies, e.g. involving additional coatings, might be required for the stable, long-term stability of steel-glass ceramic interfaces.

Having considered three different glass compositions (related to two different SOC operating temperatures) the main focus was on the dissimilar tendency to interfacial reactions and corrosion. This study provides new insights into possible evaluation of appropriate sealants materials in combination with a stainless steel. Comparison of our approach with a conventional glass/steel plate interac-

tion study will be the focus of further research, even considering experimental conditions with improved experimental assessment (i. e. dual atmosphere tests).

Declaration of Competing Interest

The authors declare that they have no known competing financial interests or personal relationships that could have appeared to influence the work reported in this paper.

Acknowledgements

This project was supported by National Science Centre Poland (NCN) Sonata Bis 8 project number 2018/30/E/ST8/00821 "High-temperature corrosion studies and development of oxidation lifetime model of alloy powders and sintered porous alloys: effects of composition and microstructure".

Data statement

The raw and processed data required to reproduce these findings cannot be shared at this time as the data also forms part of an ongoing study.

Appendix A. Supplementary material

Supplementary data to this article can be found online at https://doi.org/10.1016/j.matdes.2021.110259.

References

[1] M.C. Tucker, Progress in metal-supported solid oxide electrolysis cells: A review, Int. J. Hydrogen Energy. 45 (46) (2020) 24203–24218, https://doi.org/10.1016/j.ijhydene.2020.06.300.
[2] I. Sreedhar, B. Agarwal, P. Goyal, S.A. Singh, Recent advances in material and performance aspects of solid oxide fuel cells, J. Electroanal. Chem. 848 (2019), https://doi.org/10.1016/j.jelechem.2019.113315.
[3] C. Lenser, D. Udomsilp, N.H. Menzler, P. Holtappels, T. Fujisaki, L. Kwati, H. Matsumoto, A.G. Sabato, F. Smeacetto, A. Chrysanthou, S. Molin, Solid oxide fuel and electrolysis cells, 2019. https://doi.org/10.1016/B978-0-08-102726-4.00009-0.
[4] Q. Zhou, T.R. Bieler, J.D. Nicholas, Transient porous nickel interlayers for improved silver-based Solid Oxide Fuel Cell brazes, Acta Mater. 148 (2018) 156–162, https://doi.org/10.1016/j.actamat.2018.01.061.
[5] C. Johnson, R. Gemmen, N. Orlovskaya, Nano-structured self-assembled LaCrO3 thin film deposited by RF-magnetron sputtering on a stainless steel interconnect material, Compos. Part B Eng. 35 (2) (2004) 167–172, https://doi.org/10.1016/j.compositesb:2003.08.004.
[6] Q. Li, G. Cao, X. Zhang, G. Li, Topology optimization of the microstructure of solid oxide fuel cell cathodes, Acta Mater. 201 (2020) 278–285, https://doi.org/10.1016/j.actamat.2020.10.003.
[7] A.J. Jacobson, Materials for Solid Oxide Fuel Cells †, Chem. Mater. 22 (3) (2010) 660–674, https://doi.org/10.1021/cm902640j.
[8] I. Sreedhar, B. Agarwal, P. Goyal, A. Agarwal, An overview of degradation in solid oxide fuel cells-potential clean power sources, J. Solid State Electrochem. 24 (6) (2020) 1239–1270, https://doi.org/10.1007/s10008-020-04584-4.
[9] T. Gheno, D. Monceau, D.J. Young, Kinetics of breakaway oxidation of Fe-Cr and Fe-Cr-Ni alloys in dry and wet carbon dioxide, Corros. Sci. 77 (2013) 246–256, https://doi.org/10.1016/j.corsci.2013.08.008.
[10] S. Molin, M. Gazda, P. Jasinski, High temperature oxidation of porous alloys for solid oxide fuel cell applications, Solid State Ionics. 181 (25-26) (2010) 1214–1220, https://doi.org/10.1016/j.ssi.2010.06.049.
[11] S. Chevalier, L. Combemale, I. Popa, S. Chandra-Ambhorn, W. Chandra-Ambhorn, P. Promdirek, P. Wongpromrat, Development of sofc interconnect stainless steels, Solid State Phenom. 300 (2020) 135–156, https://doi.org/10.4028/www.scientific.net/SSP.300.135.
[12] T. Mori, R. Wepf, S.P. Jiang, Future prospects for the design of 'state-of-the-art' solid oxide fuel cells, J. Phys. Energy. (2020), https://doi.org/10.1088/2515-7655/ab8f05.
[13] O.Z. Sharaf, M.F. Orhan, An overview of fuel cell technology: Fundamentals and applications, Renew. Sustain. Energy Rev. 32 (2014) 810–853, https://doi.org/10.1016/j.rser.2014.01.012.
[14] T.C. Metcalfe, Development and Characterization of Nickel and Yttria-stabilized Zirconia Anodes for Metal-Supported Solid Oxide Fuel Cells Fabricated by Atmospheric Plasma Spraying, (2013).
[15] The Fabrication of Direct Oxidation Solid Oxide Fuel Cell Anodes Using Atmospheric Plasma Spraying by Mark Joseph Cuglietta A thesis submitted in conformity with the requirements for the degree of Doctor of Philosophy Graduate Department of Mechanical and, (2013).
[16] J. Molenda, K. Świerczek, W. Zając, Functional materials for the IT-SOFC, J. Power Sources. 173 (2) (2007) 657–670, https://doi.org/10.1016/j.jpowsour.2007.05.085.
[17] S.M. Haile, Fuel cell materials and components, Acta Mater. 51 (2003) 5981–6000, https://doi.org/10.1016/j.actamat.2003.08.004.
[18] N. Mahato, A. Banerjee, A. Gupta, S. Omar, K. Balani, Progress in material selection for solid oxide fuel cell technology: A review, Prog. Mater. Sci. 72 (2015) 141–337, https://doi.org/10.1016/j.pmatsci.2015.01.001.
[19] F.S. da Silva, T.M. de Souza, Novel materials for solid oxide fuel cell technologies: A literature review, Int. J. Hydrogen Energy. 42 (41) (2017) 26020–26036, https://doi.org/10.1016/j.ijhydene.2017.08.105.
[20] S.Y. Gómez, D. Hotza, Current developments in reversible solid oxide fuel cells, Renew. Sustain. Energy Rev. 61 (2016) 155–174, https://doi.org/10.1016/j.rser.2016.03.005.
[21] Z. Yang, Recent advances in metallic interconnects for solid oxide fuel cells, Int. Mater. Rev. 53 (1) (2008) 39–54, https://doi.org/10.1179/174328007X212526.
[22] Y. MATUS, L. DEJONGHE, C. JACOBSON, S. VISCO, Metal-supported solid oxide fuel cell membranes for rapid thermal cycling, Solid State Ionics. 176 (5-6) (2005) 443–449, https://doi.org/10.1016/j.ssi.2004.09.056.
[23] L. Han, B. Talic, K. Kwok, P.V. Hendriksen, H.L. Frandsen, Interface Fracture Energy of Contact Layers in a Solid Oxide Cell Stack, ACS Appl. Energy Mater. (2020), https://doi.org/10.1021/acsaem.9b02026.
[24] I. Antepara, I. Villarreal, L.M. Rodríguez-Martínez, N. Lecanda, U. Castro, A. Laresgoiti, Evaluation of ferritic steels for use as interconnects and porous metal supports in IT-SOFCs, J. Power Sources. 151 (2005) 103–107, https://doi.org/10.1016/j.jpowsour.2005.02.084.
[25] A. Bautista, E. Arahuetes, F. Velasco, C. Moral, R. Calabrés, Oxidation behavior of highly porous metallic components, Oxid. Met. 70 (5-6) (2008) 267–286, https://doi.org/10.1007/s11085-008-9120-3.
[26] A. Chyrkin, S.L. Schulze, J. Pirón-Abellán, W. Bleck, L. Singheiser, W.J. Quadakkers, Oxidation limited lifetime of Ni-base metal foams in the temperature range 700–900°C, Adv. Eng. Mater. 12 (2010) 873–883, https://doi.org/10.1002/adem.201000139.
[27] B. Talic, S. Molin, P.V. Hendriksen, H.L. Lein, Effect of pre-oxidation on the oxidation resistance of Crofer 22 APU, Corros. Sci. 138 (2018) 189–199, https://doi.org/10.1016/j.corsci.2018.04.016.
[28] L. Gan, T. Yamamoto, H. Murakami, Microstructure and diffusion behavior in the multilayered oxides formed on a Co–W electroplated ferritic stainless steel followed by oxidation treatment, Acta Mater. 194 (2020) 295–304, https://doi.org/10.1016/j.actamat.2020.04.048.
[29] M.K. Mahapatra, K. Lu, Seal glass for solid oxide fuel cells, J. Power Sources. 195 (21) (2010) 7129–7139, https://doi.org/10.1016/j.jpowsour.2010.06.003.
[30] M. LI, P. HOU, Improved Cr2O3 adhesion by Ce ion implantation in the presence of interfacial sulfur segregation, Acta Mater. 55 (2) (2007) 443–453, https://doi.org/10.1016/j.actamat.2006.07.047.
[31] F. Hong, D. Holland, Studies of interface reactions between glass ceramic coatings and metals, J. Non. Cryst. Solids. 112 (1-3) (1989) 357–363, https://doi.org/10.1016/0022-3093(89)90553-X.
[32] E. Panda, L.P.H. Jeurgens, E.J. Mittemeijer, Interface thermodynamics of ultra-thin, amorphous oxide overgrowths on AlMg alloys, Acta Mater. 58 (5) (2010) 1770–1781, https://doi.org/10.1016/j.actamat.2009.11.019.
[33] M.K. Mahapatra, K. Lu, Glass-based seals for solid oxide fuel and electrolyzer cells - A review, Mater. Sci. Eng. R Reports. 67 (5-6) (2010) 65–85, https://doi.org/10.1016/j.mser.2009.12.002.
[34] J.W. Fergus, Sealants for solid oxide fuel cells, J. Power Sources. 147 (1-2) (2005) 46–57, https://doi.org/10.1016/j.jpowsour.2005.05.002.
[35] F. Smeacetto, A. Chrysanthou, M. Salvo, T. Moskalewicz, F. D'Herin Bytner, L.C. Ajitdoss, M. Ferraris, Thermal cycling and ageing of a glass-ceramic sealant for planar SOFCs, Int. J. Hydrogen Energy. 36 (18) (2011) 11895–11903, https://doi.org/10.1016/j.ijhydene.2011.04.083.
[36] C. Asensio-Jimenez, L. Niewolak, H. Hattendorf, B. Kuhn, P. Huczkowski, L. Singheiser, W.J. Quadakkers, Effect of specimen thickness on the oxidation rate of high chromium ferritic steels: The significance of intrinsic alloy creep strength, Oxid. Met. 79 (2013) 15–28, https://doi.org/10.1007/s11085-012-9323-5.
[37] T. Phan, J. Rigelesaiyin, Y. Chen, A. Bastawros, L. Xiong, Metallic glass instability induced by the continuous dislocation absorption at an amorphous/crystalline interface, Acta Mater. 189 (2020) 10–24, https://doi.org/10.1016/j.actamat.2020.02.038.
[38] X. Guo, Y. Zhang, Y.G. Jung, L. Li, J. Knapp, J. Zhang, Ideal tensile strength and shear strength of ZrO2(111)/Ni(111) ceramic-metal Interface: A first principle study, Mater. Des. 112 (2016) 254–262, https://doi.org/10.1016/j.matdes.2016.09.073.
[39] B. Kaur, K. Singh, O.P. Pandey, Microstructural study of Crofer 22 APU-glass interface for SOFC application, Int. J. Hydrogen Energy. 37 (4) (2012) 3839–3847, https://doi.org/10.1016/j.ijhydene.2011.04.160.
[40] D.A. Krainova, N.S. Saetova, A.S. Farlenkov, A.V. Khodimchuk, I.G. Polyakova, A. V. Kuzmin, Long-term stability of SOFC glass sealant under oxidising and reducing atmospheres, Ceram. Int. (2020), https://doi.org/10.1016/j.ceramint.2020.12.019.
[41] I. Ritucci, K. Agersted, P. Zielke, A.C. Wulff, P. Khajavi, F. Smeacetto, A.G. Sabato, R. Kiebach, A Ba-free sealing glass with a high coefficient of thermal expansion and excellent interface stability optimized for SOFC/SOEC stack applications,

Int. J. Appl. Ceram. Technol. 15 (2018) 1011–1022, https://doi.org/10.1111/ijac.12853.
[42] P. Piccardo, A. Pecunia, V. Bongiorno, R. Spotorno, Z. Wuillemin, J.P. Ouweltjes, Ageing of Materials at Inlet and Outlet Fuel Manifolds in a SOFC Stack, ECS Trans. 68 (1) (2015) 2611–2624, https://doi.org/10.1149/06801.2611ecst.
[43] S. Rodríguez-López, J. Wei, K.C. Laurenti, I. Mathias, V.M. Justo, F.C. Serbena, C. Baudín, J. Malzbender, M.J. Pascual, Mechanical properties of solid oxide fuel cell glass-ceramic sealants in the system BaO/SrO-MgO-B2O3-SiO2, J. Eur. Ceram. Soc. 37 (11) (2017) 3579–3594, https://doi.org/10.1016/j.jeurceramsoc.2017.03.054.
[44] K. Raju, Muksin, S. Kim, K.-S. Song, J.H. Yu, D.-H. Yoon, Joining of metal-ceramic using reactive air brazing for oxygen transport membrane applications, Mater. Des. 109 (2016) 233–241, https://doi.org/10.1016/j.matdes.2016.07.068.
[45] T.S. Lumpe, J. Mueller, K. Shea, Tensile properties of multi-material interfaces in 3D printed parts, Mater. Des. 162 (2019) 1–9, https://doi.org/10.1016/j.matdes.2018.11.024.
[46] R. Harizanova, R. Keding, C. Rüssel, Electric conductivity of glasses in the system Na2O/CaO/SiO2/Fe2O3, J. Non. Cryst. Solids. 354 (1) (2008) 65–71, https://doi.org/10.1016/j.jnoncrysol.2007.07.014.
[47] R.N. Singh, High-temperature seals for Solid Oxide Fuel Cells (SOFC), J. Mater. Eng. Perform. 15 (4) (2006) 422–426, https://doi.org/10.1361/105994906X117224.
[48] H. Elsayed, H. Javed, A.G. Sabato, F. Smeacetto, E. Bernardo, Novel glass-ceramic SOFC sealants from glass powders and a reactive silicone binder, J. Eur. Ceram. Soc. 38 (12) (2018) 4245–4251, https://doi.org/10.1016/j.jeurceramsoc.2018.05.024.
[49] X.-V. Nguyen, C.-T. Chang, G.-B. Jung, S.-H. Chan, W.-T. Lee, S.-W. Chang, I.-C. Kao, Study of sealants for SOFC, Int. J. Hydrogen Energy. 41 (46) (2016) 21812–21819, https://doi.org/10.1016/j.ijhydene.2016.07.156.
[50] P. Batfalsky, V.A.C. Haanappel, J. Malzbender, N.H. Menzler, V. Shemet, I.C. Vinke, R.W. Steinbrech, Chemical interaction between glass-ceramic sealants and interconnect steels in SOFC stacks, J. Power Sources. 155 (2) (2006) 128–137, https://doi.org/10.1016/j.jpowsour.2005.05.046.
[51] Y.-S. Chou, J.W. Stevenson, J.-P. Choi, Alkali Effect on the Electrical Stability of a Solid Oxide Fuel Cell Sealing Glass, J. Electrochem. Soc. 157 (2010) B348, https://doi.org/10.1149/1.3275744.
[52] R. Li, L. Peng, X. Wang, J. Yang, D. Yan, J. Pu, B. Chi, J. Li, Investigating the performance of Glass/Al2O3 composite seals in planar solid oxide fuel cells, Compos. Part B Eng. 192 (2020), https://doi.org/10.1016/j.compositesb.2020.107984 107984.
[53] H. Javed, A.G. Sabato, K. Herbrig, D. Ferrero, C. Walter, M. Salvo, F. Smeacetto, Design and characterization of novel glass-ceramic sealants for solid oxide electrolysis cell (SOEC) applications, Int. J. Appl. Ceram. Technol. 15 (2018) 999–1010, https://doi.org/10.1111/ijac.12889.
[54] T. Zhang, H. Zhang, G. Li, H. Yung, Reduction of chromate formation at the interface of solid oxide fuel cells by different additives, J. Power Sources. 195 (19) (2010) 6795–6797, https://doi.org/10.1016/j.jpowsour.2010.04.060.
[55] T. Zhang, R.K. Brow, W.G. Fahrenholtz, S.T. Reis, Chromate formation at the interface between a solid oxide fuel cell sealing glass and interconnect alloy, J. Power Sources. 205 (2012) 301–306, https://doi.org/10.1016/j.jpowsour.2012.01.043.
[56] G. Sander, D. Jiang, Y. Wu, N. Birbilis, Exploring the possibility of a stainless steel and glass composite produced by additive manufacturing, Mater. Des. 196 (2020), https://doi.org/10.1016/j.matdes.2020.109179.
[57] M. Ferraris, S. De la Pierre, A.G. Sabato, F. Smeacetto, H. Javed, C. Walter, J. Malzbender, Torsional shear strength behavior of advanced glass-ceramic sealants for SOFC/SOEC applications, J. Eur. Ceram. Soc. 40 (12) (2020) 4067–4075, https://doi.org/10.1016/j.jeurceramsoc.2020.04.034.
[58] F.A. Stevie, R. Garcia, J. Shallenberger, J.G. Newman, C.L. Donley, Sample handling, preparation and mounting for XPS and other surface analytical techniques, J. Vac. Sci. Technol. A. 38 (2020), https://doi.org/10.1116/6.0000421 063202.
[59] G.H. Major, N. Fairley, P.M.A. Sherwood, M.R. Linford, J. Terry, V. Fernandez, K. Artyushkova, Practical guide for curve fitting in x-ray photoelectron spectroscopy, J. Vac. Sci. Technol. A. 38 (2020), https://doi.org/10.1116/6.0000377 061203.
[60] J.W. Fergus, Metallic interconnects for solid oxide fuel cells, Mater. Sci. Eng. A. 397 (1-2) (2005) 271–283, https://doi.org/10.1016/j.msea.2005.02.047.
[61] H. Javed, A.G. Sabato, I. Dlouhy, M. Halasova, E. Bernardo, M. Salvo, K. Herbrig, C. Walter, F. Smeacetto, Shear performance at room and high temperatures of glass-ceramic sealants for solid oxide electrolysis cell technology, Materials (Basel). 12 (2019), https://doi.org/10.3390/ma12020298.
[62] L. Peng, Q. Zhu, Thermal cycle stability of BaO – B 2 O 3 – SiO 2 sealing glass, 194 (2009) 880–885. https://doi.org/10.1016/j.jpowsour.2009.06.018.
[63] M.J. Pascual, A. Guillet, A. Dur, Optimization of glass – ceramic sealant compositions in the system MgO – BaO – SiO 2 for solid oxide fuel cells (SOFC), ☙ 169 (2007) 40–46, https://doi.org/10.1016/j.jpowsour.2007.01.040.
[64] M.C. Biesinger, C. Brown, J.R. Mycroft, R.D. Davidson, N.S. McIntyre, X-ray photoelectron spectroscopy studies of chromium compounds, Surf. Interface Anal. 36 (12) (2004) 1550–1563, https://doi.org/10.1002/(ISSN)1096-9918.
[65] M. Aronniemi, J. Sainio, J. Lahtinen, Chemical state quantification of iron and chromium oxides using XPS: The effect of the background subtraction method, Surf. Sci. 578 (2005) 108–123, https://doi.org/10.1016/j.susc.2005.01.019.
[66] J.H. Ryu, J.H. Yang, J.J. Yoh, A non-calorimetric approach for investigating the moisture-induced ageing of a pyrotechnic delay material using spectroscopies, Sci. Rep. 9 (2019) 1–11, https://doi.org/10.1038/s41598-019-51667-y.
[67] A.G. Sabato, A. Rost, J. Schilm, M. Kusnezoff, M. Salvo, A. Chrysanthou, F. Smeacetto, Effect of electric load and dual atmosphere on the properties of an alkali containing diopside-based glass sealant for solid oxide cells, J. Power Sources. 415 (2019) 15–24, https://doi.org/10.1016/j.jpowsour.2019.01.051.
[68] M. Stanislowski, E. Wessel, K. Hilpert, T. Markus, L. Singheiser, Chromium Vaporization from High-Temperature Alloys, J. Electrochem. Soc. 154 (2007) A295, https://doi.org/10.1149/1.2434690.
[69] E.J. Opila, D.L. Myers, N.S. Jacobson, I.M.B. Nielsen, D.F. Johnson, J.K. Olminsky, M.D. Allendorf, Theoretical and experimental investigation of the thermochemistry of CrO2(OH)2(g), J. Phys. Chem. A. 111 (10) (2007) 1971–1980, https://doi.org/10.1021/jp064738010.1021/jp0647380.s001.
[70] J.R.J.R. C.D. Wagner, A.V. Naumkin, A. Kraut-Vass, J.W. Allison, C.J. Powell, NIST Standard Reference Database 20, Version 4.1 (web version) (http:/srdata.nist.gov/xps/), 2012. https://doi.org/10.18434/T4T88K.
[71] K.D. Moulder, J.F; Stickle, W. F; Sobol, P. E; Bomben, Handbook of X-ray Photoelectron Spectroscopy, Perkin-Elmer Corp., Eden Prairie, MN, 1992.
[72] K. Sood, J. Kaswan, S.P. Singh, T. Norby, S. Basu, 6 Na 0 (2018) 3009–3013, https://doi.org/10.1007/s10008-018-4007-y.